The Remote Role of North-American Mesoscale Convective Systems on the Forecast of a Rossby Wave Packet: A Multi-Model Ensemble Case-study

Alexander Lojko[1], Ashley Payne[1,2], Christiane Jablonowski[1]

[1]Department of Climate and Space Sciences and Engineering, University of Michigan, Ann Arbor, MI 48109-2143, USA
[2]Tomorrow.io, Boston, MA 02210, USA

Key Points:

- Global forecasting models struggle to realistically represent negative potential vorticity arising from mesoscale convective systems.
- Anticyclonic circulation errors associated with negative potential vorticity introduce rotational wind errors into the jet stream.
- Jet stream errors associated with negative potential vorticity modify the phasing and forecast skill of a Rossby-wave packet.

Corresponding author: Alexander Lojko, `alojko@umich.edu`

Abstract

North American Mesoscale Convective Systems (MCSs) have been linked to instances of poorly forecasted Rossby wave packets. A computationally inexpensive investigation is proposed to demonstrate a dynamical mechanism by which MCSs modify a Rossby wave packet associated with a high-impact weather event. Global ensemble forecast data, reanalysis and high-resolution observations are used to assess the remote role of negative potential vorticity (PV) arising from divergent outflow on Rossby wave packet (RWP) propagation coinciding with the June 11th - 21st, 2017 European heatwave. In this case, synoptic-scale bands of negative PV which advect towards the jet stream arise from regions of active MCSs. The forecast data results show that the numerical misrepresentation of the anticyclonic circulation associated with negative PV can impinge on the forecast of a RWP. In each of the four forecasting models assessed, ensemble members that advected lower values of PV towards the equatorward branch of a North American ridge favored enhanced poleward amplification of the ridge and a more eastward progression of the RWP. The more eastward displacement of the RWP also coincided with an enhanced wave activity flux downstream. Although, we do not find a significant impact on the forecasted heatwave. The results urge further investigation into the role of negative PV in remotely influencing high-impact weather.

Plain Language Summary

Large severe thunderstorms over North America have been observed to occasionally precede poor forecasts over Europe. In this case-study, we use state-of-the-art weather model data and observations to provide a process-level understanding of how thunderstorms modify the evolution of the jet stream. The case selected coincides with the June 11th - 21st, 2017 European heatwave. Our study shows that air with a signature of intense clockwise circulation arises from the cloud-tops of severe thunderstorms and rapidly expands onto synoptic-scales (1000 km). In the four weather models assessed; there is a persistent bias in the representation of how this synoptic-scale, clockwise air interacts with the jet stream over North America. The erroneous interaction introduces forecast error into the jet stream and significantly modifies its down wind evolution over the Atlantic. However, we did not note a significant impact on the forecasted heatwave in this case. The results obtained in this study warrant further investigation on the role of thunderstorms in influencing the jet stream and European weather.

1 Introduction

Rossby-wave packets consist of a propagating collection of troughs and ridges along the jet stream. Instances of temperature extremes in the mid-latitudes have been linked to highly amplified, and temporally persistent Rossby-wave packets (RWPs; Fragkoulidis et al., 2018; Röthlisberger et al., 2019; Ali et al., 2021), including recent prolific European heatwaves (Fragkoulidis et al., 2018; Zschenderlein et al., 2018). Despite their role in triggering high-impact weather, RWPs can still be a challenge for numerical weather prediction (NWP) models to realistically simulate (Gray et al., 2014; Grazzini & Vitart, 2015; Quinting & Vitart, 2019). Advancing understanding of the dynamical precursors that impinge upon the forecast of troughs and ridges is paramount to disseminate sources of NWP uncertainty for future forecasts of high-impact weather.

Divergent outflow arising from organized, diabatic weather systems (i.e., Tropical cyclones, Warm-Conveyor Belts, Mesoscale Convective Systems) serves as a critical mechanism for rapid upscale error growth (Zhang et al., 2003; Baumgart et al., 2018) and thus in the generation

of NWP uncertainty (Rodwell & Wernli, 2022). Divergent outflow can
modify the amplitude of a ridge and enhance adjacent wind speeds via
the poleward advection of diabatically heated air along the tropopause
(Archambault et al., 2015; Riboldi et al., 2018; Keller et al., 2019; Stuivenvolt Allen et al., 2021).
Subsequently, these perturbations to the large-scale flow can modulate the down-
stream dispersion of Rossby waves (Gray et al., 2014; B. J. Harvey et al., 2016).
However, global NWP models have been noted to misrepresent
the magnitude of divergent outflow due to initial condition error
(Rodwell et al., 2018; Magnusson et al., 2019) and the necessity to pa-
rameterize diabatic sub-grid scale processes such as latent heat release
(Martínez-Alvarado et al., 2016; Joos & Forbes, 2016). Thus, upscale error
growth associated with divergence can impinge upon downstream forecast skill
(Grams et al., 2015; Lillo & Parsons, 2017; Baumgart et al., 2018; Keller et al., 2019; Clarke et al., 2019).

The impact of divergent outflow on jet stream dynamics has often been facil-
itated through the potential vorticity (PV) perspective (Hoskins et al., 1985). On
synoptic-scales, divergent outflow leads to a net reduction of PV at the tropopause,
which is driven by the vertical gradient of diabatic heating (Wernli & Davies, 1997).
Advection of diabatically reduced PV by divergent winds towards the jet stream
can facilitate a RWP response (Riemer et al., 2008; Archambault et al., 2015).
However, at scales where the Rossby number is larger than unity, the hor-
izontal gradient of diabatic heating becomes significant in modifying PV
(Chagnon & Gray, 2009; Weijenborg et al., 2015, 2017; Oertel et al., 2020). In lo-
calized regions (spatial scales of 10's of kilometers) characterized by a convective
updraft and strong vertical wind shear, PV dipoles on the order of +/- 10 PVU are
observed to form at the tropopause (Weijenborg et al., 2015; Oertel et al., 2020).
The horizontal heating gradient is the mechanism which can turn PV nega-
tive (in the Northern Hemisphere)(B. Harvey et al., 2020). . Strong wind
shear near the jet stream elongates and dillutes PV dipoles onto synoptic-
scales. Recent studies have shown that the interaction of the elongated nega-
tive PV pole with the jet stream can influence its in-situ dynamical structure
(Chagnon et al., 2013; Oertel et al., 2020; B. Harvey et al., 2020; Prince & Evans, 2022).

Strong vertical wind shear and pronounced divergent outflow that
can alter the upper-level flow can occur with mesoscale convective sys-
tems (MCSs) (Tung & Yanai, 2002; Houze, 2004). Early literature on this
topic demonstrates that MCS activity near the jet stream is often fol-
lowed by ridge amplification and the production of an adjacent jet streak
(Maddox, 1983; Cotton et al., 1989; Anderson & Arritt, 1998). Temporally
prolonged MCS activity has also been proposed to potentially modify large-
scale circulation patterns in the mid-latitudes (Stensrud & Anderson, 2001).
Clarke et al. (2019) provide a recent case-study of an MCS over the UK am-
plifying downstream development. The authors deduced that the advection
of a convectively generated negative PV pole towards the jet stream serves as
a crucial mechanism for the modification of downstream development. These
findings are particularly relevant for North American MCSs, which, aside
from typically producing stronger divergent outflow than MCSs over the UK,
have also been observed to precede sudden drops in forecast skill over Europe
(Rodwell et al., 2013; Lillo & Parsons, 2017; Rodwell et al., 2018; Parsons et al., 2019).

Given the potential for MCSs to influence the downstream propagation of
RWPs and their crucial link to drops in operational weather forecasting skill, a
process-level investigation is performed to deduce the impact of a North Ameri-
can MCS on the downstream propagation and forecast-skill of a RWP. A unique
approach taken in this study is to assess the downstream impact of an MCS using
global ensemble forecast data from multiple different models. This approach en-

ables an examination of whether the misrepresentation of the interaction between MCSs and RWPs is consistent in different weather prediction models. The study focuses on the dynamical development of a RWP that coincides with the June 2017 European heatwave, which occurred from the 11th – 21st of June 2017 (Sánchez-Benítez et al., 2018) and was preceded by a series of MCSs over the United States several days prior. The event was also associated with amplified recurring RWPs, providing an analogous case to other recent heatwaves associated with recurring RWPs (Zschenderlein et al., 2018). The paper structure follows: Section 2 describes the methodology and datasets, Section 3 gives a synoptic-scale and forecast skill overview, Section 4 provides the case-study results, and Section 5 is a discussion and conclusion of the work.

2 Data and Methods

2.1 Data

The ECMWF reanalysis version 5 (ERA5; Hersbach et al., 2020), downloaded at a 0.25° (~31 km) grid resolution, is used to observationally analyze synoptic-scale and larger mesoscale (i.e., MCSs) dynamics. ERA5 is ideal for this purpose due to its global coverage and high temporal resolution (hourly). ERA5 has also been found to validate well against satellite observations when analyzing the spatial location of mesoscale cloud structures such as those arising from warm-conveyor belts (Binder et al., 2020).

To supplement ERA5 data, MCS activity over the contiguous United States is tracked and assessed using a database created from the FLEXible object TRaKeR (FLEXTRKR) algorithm (Feng et al., 2018) from 2004-2017 at an hourly ~0.04° (4 km) grid resolution (Feng et al., 2019). The database combines NASA Global Merged infrared brightness temperature satellite data (Janowiak et al., 2001), GridRad 3D NEXRAD radar data (Cooney et al., 2018) and NCEP Stage IV precipitation data (Lin, 2011) to provide information on the life-cycle and characteristics of MCSs. The algorithm classifies an MCS as a precipitating cloud system with an area $> 6\times10^4$ km^2 and a major axis length > 100 km, a radar reflectivity value > 45 dBz and assesses whether the precipitating cloud persists for at least 6 hours.

Forecast data is analyzed using perturbed ensemble forecast data from the European Centre for Medium-Range Weather Forecasting (ECMWF), Japanese Meteorological Agency (JMA), National Center for Environmental Protection (NCEP) and the Korean Meteorological Agency (KMA) stored within 'The International Grand Global Ensemble' (TIGGE) archive (Swinbank et al., 2016). The perturbed members are used to assess ensemble spread. The analysis from each forecast center is used to assess the forecast skill of the perturbed members. Forecast data is downloaded for the month of June 2017 from 6-hourly forecasts initialized each day at 00 UTC. Further details regarding the archived model data from each ensemble prediction system are presented in Table 1.

2.2 Forecast Skill Analysis

2.2.1 Root Mean Square Error

To assess forecast skill over Europe, the area-weighted, spatially averaged, root mean squared error (RMSE) is computed using geopotential height fields at 250 hPa (Z250) over Europe (35°N, 12.5°W) – (75°N, 42.5°E). The equation used to compute the RMSE over the European domain is shown in Equation (1). The European domain is visualized in Fig. 1.

–4–

Table 1. TIGGE Model Configurations[a] for each modeling center (left most column). Native, archived and interpolated horizontal resolutions are listed in the center columns and the total number of available ensemble members is in the right most column.

Center	Native	Archived	Interpolated	Members
ECMWF	$0.14° \times 0.14°$ *N640L91*	$0.56° \times 0.56°$	$1.0° \times 1.0°$	50
JMA	$0.36° \times 0.36°$ *TL479L100*	$1.25° \times 1.25°$	$1.0° \times 1.0°$	26
NCEP	$0.3° \times 0.3°$ *TL574L64*	$1.0° \times 1.0°$	$1.0° \times 1.0°$	20
KMA	$0.83° \times 0.56°$ *N216L85*	$0.83° \times 0.56°$	$1.0° \times 1.0°$	24

[a] L = number of vertical levels. T = highest wave number resolved in spherical harmonics (note that all model analysis is interpolated onto grid-point space). N = number of grid points from equator to pole.

$$RMSE = \sqrt{\frac{1}{N_{Total}} \sum_{i=1}^{N_{Total}} (Z250_e)^2} \qquad (1)$$

where $Z250_e$ denotes the difference between the ensemble mean of the day 6 perturbed forecast members and the corresponding analysis as a measure of truth. The RMSE is calculated for all grid-points, N_{Total}, in the European domain and the mean is computed. This includes an area weight which has been left out in Equation (1) for simplicity. The calculations are performed at 24-hour intervals with all forecasts initialized at 00 UTC spanning June 1st – 24th 2017. The RMSE has units of meters and is calculated independently for each of the four models.
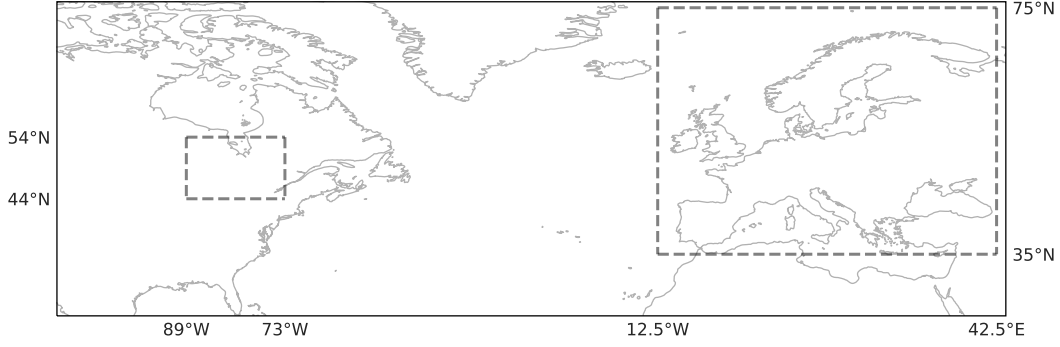
–5–

Figure 1. Schematic indicating averaging regions when analyzing forecast data. The large box over Europe (35°N, 12.5°W) – (75°N, 42.5°E) is termed the European domain. This area is used for spatially averaged RMSE analysis. This region is also used to focus on the ridge amplification event over Europe. The boxed region over North America (54°N, 89°W) – (44°N, 73°W) is the averaged region used for studying the impacts of jet stream wind error on the downstream development of a RWP.

2.2.2 Amplitude Error and Wave Activity Flux

A (wave) amplitude error metric (WAE: Parsons et al., 2019) is applied to examine the downstream propagation of error induced by the initial misrepresentation of the RWP and its subsequent impacts on the dynamics and forecast skill over Europe. The metric used in equation (2) is phase independent and tracks packets of error that propagate in a wave-like motion (i.e., RWPs) and specifically pertains to rotational error due to the use of the streamfunction term. This makes the metric useful for identifying the initial development of forecast error onto the jet stream, which is dominated by non-divergent wind flow (Keyser & Johnson, 1984; Winters, 2021).

$$WAE_\psi = \frac{1}{2}\left[\left(\frac{\partial \psi_e}{\partial x}\right)^2 + \left(\frac{\partial \psi_e}{\partial y}\right)^2 - \psi_e\left(\frac{\partial^2 \psi_e}{\partial x^2} + \frac{\partial^2 \psi_e}{\partial y^2}\right)\right] \quad (2)$$

In Equation 2, ψ_e denotes the streamfunction error calculated from the horizontal wind field at 250 hPa. The streamfunction is computed in spherical coordinates using the Windspharm Python package (Dawson, 2016). As with Equation 1, wind forecast error is calculated at each grid-point as the difference between the analysis and the corresponding mean of the perturbed forecast members. Converting all terms into streamfunction terms aids in the interpretation of Equation 2. Consider the form of a 2d plane wave, $\psi_e = \psi_{e0}sin(kx + ly)$ where k and l are the horizontal wavenumbers in the zonal and meridional directions. Inputting the plane wave term into Equation 2 simplifies the equation to: $WAE = \frac{1}{2}\psi_{e0}^2(k^2 + l^2)$. Thus the metric can be interpreted as the amplitude of rotational errors scaled by the total wave number (Parsons et al., 2019).

To compliment understanding in the error that propagates within a RWP, the wave activity flux (WAF) is computed following Takaya and Nakamura (2001) and reformulated in streamfunction terms as in Parsons et al. (2019). The WAF enables tracking of small amplitude quasi-geostrophic eddies along a zonally varying basic flow. The WAF is computed on a single vertical level of 250 hPa at each individ-

–6–

ual forecast time. Hence, in Equation 3, the WAF metric assumes a stationary and two-dimensional wave.

$$\overrightarrow{W_e} = \frac{1}{2|\vec{U}|} \left(\begin{array}{c} U[(\frac{\partial \psi_e}{\partial x})^2 - \psi_e \frac{\partial^2 \psi_e}{\partial x^2}] + V[\frac{\partial \psi_e}{\partial x}\frac{\partial \psi_e}{\partial y} - \psi_e \frac{\partial^2 \psi_e}{\partial x \partial y}] \\ U[\frac{\partial \psi_e}{\partial x}\frac{\partial \psi_e}{\partial y} - \psi_e \frac{\partial^2 \psi_e}{\partial x \partial y}] + V[(\frac{\partial \psi_e}{\partial y})^2 - \psi_e \frac{\partial^2 \psi_e}{\partial y^2}] \end{array} \right) \tag{3}$$

The U and V terms denote the average zonal and meridional wind velocity computed between the analysis and the forecasted ensemble mean. The $|\vec{U}|$ term denotes the average wind speed magnitude from the combination of U and V terms.

2.2.3 Ensemble Sensitivity Analysis

Using an ensemble of 'i' members that make up a forecast, ensemble sensitivity analysis (ESA; Torn & Hakim, 2008) is applied to deduce the impact of different ensemble realizations of RWP initiation over North America on the evolution of the forecast of the European ridge.

ESA is a linear regression correlation method used to identify relationships between geographically distanced dynamical phenomena using different forecast lead times and forecast variables. In this case, ESA is used to deduce the statistical correlation between the role of RWP initiation over North America on its downstream development. The ESA technique applied in this study follows from Magnusson (2017):

$$Corr.(x, y) = cov \frac{(J_i, F_{ixy})}{\sigma(J_i)\sigma(F_{ixy})} \tag{4}$$

Equation 4 shows how a forecast field (Z250), termed F at grindpoint (x, y), responds to a spatially averaged forecast metric, J, at an earlier forecast lead-time over the North-American domain (Fig. 1). In this case, the J is the wave amplitude error over the North American domain (WAE) at forecast-time day 2. The i term denotes the ensemble member while x and y are the latitude and longitude grid points. The *cov* term denotes the covariance which is calculated between J and F. σ is the ensemble standard deviation and is used to normalize against the covariance to obtain a dimensionless correlation between J and F.

While the technique assumes linearity between the two variables, the method is capable of illuminating correlations between highly non-linear weather events (Chang et al., 2013; Quandt et al., 2019). The correlations are determined to be statistically significant via the computation of a Student's t-test performed at the 95% confidence interval. For the ECMWF (50 members), JMA (26 members), NCEP (20 members) and KMA (24 members), a correlation at a grid-point must have values of 0.28, 0.4, 0.47 and 0.42 respectively to be statistically significant. The study seeks to improve the robustness of ESA by utilizing TIGGE for a multi-model ESA. The multi-model analysis serves to alleviate instances of spurious sensitivity. If all four models converge to a spatially similar and strongly correlated sensitivity pattern, this will improve confidence in the reliability of the ESA results.

3 Case Overview

This study provides an atmospheric dynamics examination and forecast skill perspective of the role that MCSs have in the onset of a ridging event over Europe that coincided with a heatwave (Sánchez-Benítez et al., 2018). In Figure 2a, temporally averaged Z250 from 06/11 - 06/21 00 UTC (the times associated with heatwave

onset, maturity and decay; Sánchez-Benítez et al., 2018) show a persistent and positive Z250 anomaly over Western Europe in excess of 200 m. Note the undulation of positive and negative Z250 anomalies that track back to North America; a signature of an amplified jet stream during this time-period. The mean 06/11 - 06/21 850 hPa wind velocity vectors over North America show a strong and poleward low-level jet orientated towards the left flank of a positive Z250 anomaly. This synoptic set-up is conducive to the development of persistent MCSs over the Central Great Plains (Maddox, 1983; Anderson & Arritt, 1998; Yang et al., 2017) and and has previously been identified as a weather pattern that precedes instances of reduced forecast skill over Europe (Rodwell et al., 2013).

The 6-hourly Hovmöller diagram of 250 hPa meridional winds in Fig. 2b similarly shows persistent RWP activity (alternation of positive and negative velocity) that propagates towards Europe. Once the positive meridional velocity component of the RWP reaches the Eastern Atlantic, there is a subsequent increase in the 850 hPa June temperature anomaly over Western Europe. This is most notable on 06/16 - 06/18 and is linked to the emergence of a RWP 110°W on the 06/13.

Figure 3 displays the day 6 RMSE analysis over Europe for Z250 during the June 2017 time-period. The subset of June forecasts are characterized by two peaks in RMSE. The first peak is associated with the forecasts initialized on 06/06 and 06/07, which corresponds to the time-period just before a RWP is initiated over North America on 06/08 at 100°W. The larger peak in RMSE occurs on 06/12 and 06/13, which also occurs prior to the downstream propagation of a RWP. The average RMSE reaches values in excess of 120 m over Europe and is the highest for the entirety of the month of June.

Both days are associated with a large range of RMSE values. The KMA model performs particularly poorly during this time-period, with RMSE values in excess of 140 m on the 06/13 for most ensemble members. Further analysis examines the forecast initialized on 06/12 where all four models indicate large ensemble spread in forecast skill. Sufficiently large ensemble spread will improve the quality of the ESA performed later on in the study.
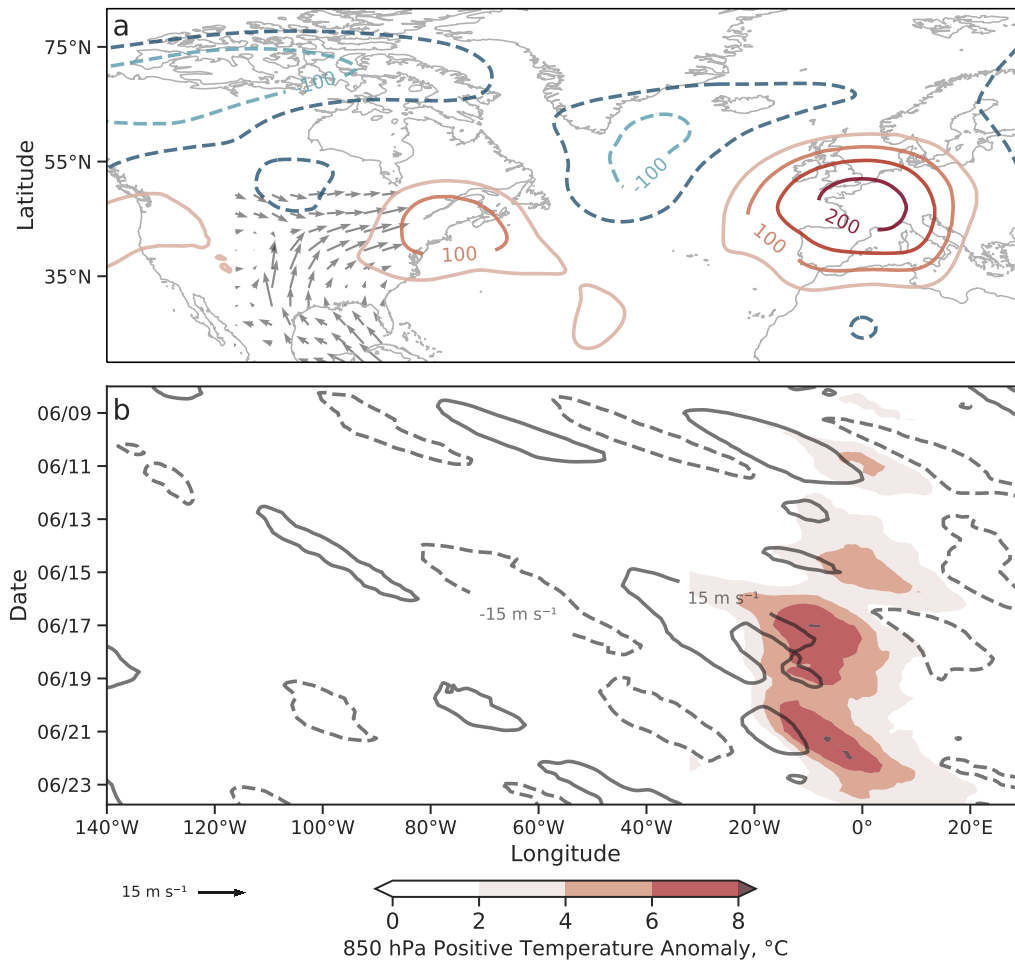
Figure 2. The top panel (a) shows the temporally averaged fields from the 06/11 - 06/21. The red and blue contours show positive and negative Z250 anomalies with respect to the June climatology (1981 – 2020). Contours are made at intervals of 50 m. The vectors show the mean 850 hPa winds over CONUS during 06/11 - 06/21. The maxima in the vectors indicate values of 15 m s^{-1}. The bottom panel (b) shows a Hovmöller of 250 hPa meridional winds with an area-weighted average taken over 35° - 65°N. Solid (dashed) contours indicate positive (negative) values of 15 m s^{-1}. The red shading indicates positive temperature anomalies with respect to the June climatology at 850 hPa.
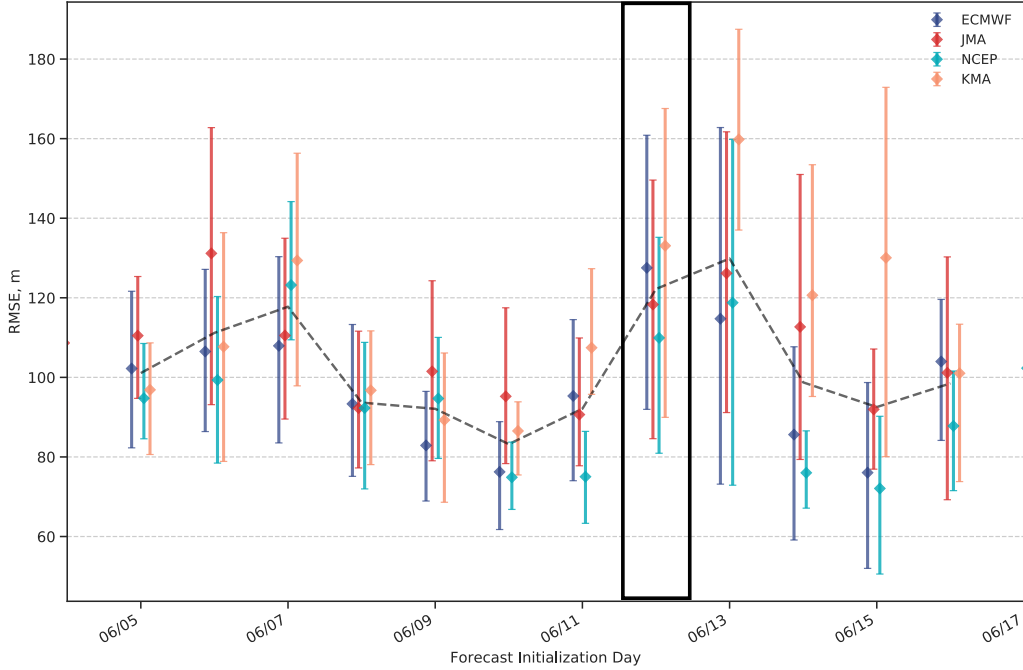
Figure 3. Forecast day-6 Z250 area-weighted RMSE for the European domain (35°N, 12.5°W) – (75°N, 42.5°E) for each of the four forecasting models. The colored dots indicate the mean RMSE of the ensemble for each model, the top and bottom of the lines indicate the 80$^{\text{th}}$ and 20$^{\text{th}}$ RMSE percentiles, respectively. The black dashed line is the mean RMSE calculated for all four of the models. The models are all initialized at 00 UTC for the respective days in the x-axis. Hence, for a forecast initialized on 06/11 00 UTC, the RMSE plot represents the outcome for 06/17 00 UTC. The black rectangle on 06/12 indicates the selected forecast for further analysis.

4 Results

4.1 Wave Amplitude Error Analysis

Motivated by the extension of a RWP from North America into Europe, we use the wave amplitude error (WAE) metric in order to identify the origin of the RWP forecast error and the WAF error metric to illustrate the directional component of the error packet. The metrics are applied to forecasts initialized at 00 UTC 06/12. The band of amplitude error emerges in the exact same location along the jet stream in each of the 4 forecasting models. For this reason, a single mean WAE is computed for all four models.

In Fig. 4, the WAE is shown at 250 hPa for different forecast lead-times. At day 6 in the forecast (Fig. 4a), the location of WAE maxima is predominantly associated with the poleward extension of the ridge over Europe. The metric indicates maxima in wind rotational errors about the axis of the ridge's anticyclonic tilt (as observed in the Z250 analysis contours). A maxima in the WAF error is also observed and overlain over the WAE maxima. The eastward orientation of the error implies that the analysis produces a stronger downstream WAF compared to the day 6 forecast. Furthermore, much of the WAE coincides with the leading edge of the 50 m s^{-1} wind velocity contour (see the orange dashed contour), indicating that the forecasting models struggle with realistically representing rotational winds embed-

–10–

ded within jet stream. However, this area is also associated with large streamline gradients, hence minor displacements in the location of streamlines between forecast and analysis will serve to magnify the WAE metric compared to regions with more slack wind condition. The WAE also embeds itself within the adjacent low-pressure system at approximately 20°E implying that the erroneous RWP impinges on the adjacent cyclogensis.

Tracking back to day 4 (Fig. 4b), the maxima in the amplitude error is located over the Atlantic associated with the poleward branch of the developing ridge. The WAE packet is co-located precisely with the 50 m s^{-1} wind velocity contour, which indicates that the synoptic-scale wind velocity maxima in the propagating RWP is not being accurately resolved by day 4 in the forecast. We note that the metric appears to highlight erroneous model performance where strong gradients in the streamlines develop. The upstream location of the WAE packet with respect to forecast day 6, in addition to the eastward orientation of the WAF error, also indicates an eastward propagating error with respect to forecast lead-time.

The first packet of WAE that can be clearly resolved at 1 degree resolution emerges at forecast day 2 (Fig. 4c) as a mesoscale disturbance on the equatorward side of the 50 m s^{-1} jet stream velocity contour. An eastward orientated WAF error emphasizes that the forecasting models struggle with representing the magnitude of downstream eddy propagation along the ridge. The location of the WAE packet is consistent in all four of the models. The WAE is also associated with notable ensemble spread which indicates that some ensemble members produce less rotational wind error than others. The initiation of the WAE packet coincides with the emergence of the RWP over North America discussed in Fig. 2b. An erroneous WAF in excess of 100 m^2 s^{-1} also develops alongside the packet of WAE. Given that all models trigger an erroneous packet of error along the equatorward branch of the ridge, the next section examines whether there is a consistent dynamic mechanism that leads to the manifestation of the error.
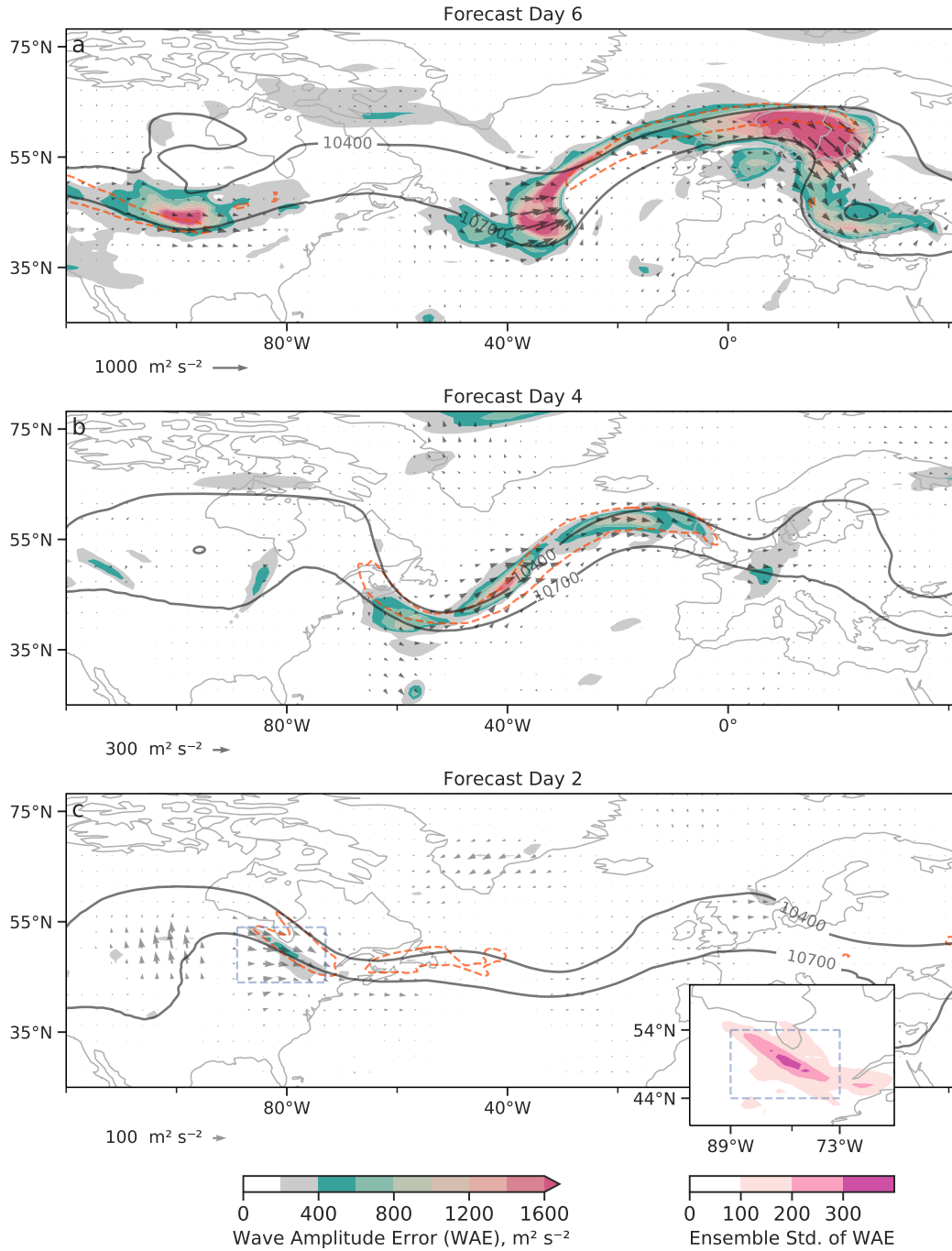
Figure 4. 250 hPa analysis of the wave amplitude error metric computed from the mean of all four ensemble members with the forecast initialized on 06/12 00 UTC. Larger values of wave amplitude error indicate increased departure from the analysis. Vectors show the wave activity flux error which is also computed from the mean of all four ensemble members. Orange contours denote the analysis wind speed at 50 m s^{-1}. The two black contours are the 10400 and 10700 m geopotential height lines at 250 hPa. Panel a, b and c shows forecasts times day 6, 4 and 2 respectively.

4.2 Dynamics over North America: Reanalysis and Observations

Having traced back the earliest instance of WAE associated with an uncertain RWP, we use reanalysis and observations to examine the relevant dynamic processes that are co-located with the amplification of the RWP over North America. In combination with MCS observations from FLEXTRKR, we use Ertel's potential vorticity derived from ERA5 to track contours of 0 potential vorticity units (PVU) at 250 hPa. Negative PV is observed to arise from the horizontal gradient of diabatic heating in environments characterized by vigorous convective updrafts and pronounced vertical wind shear. Hence 0 PVU is used as a proxy to track the advection of diabatically modified air influenced by the horizontal gradient of heating from convective updrafts within MCSs. The specific mechanism for negative PV production is outlined in B. Harvey et al. (2020). Note for simplicity in the analysis below, the term jet streak is used to describe wind speeds in excess of 50 m s^{-1}.

Figure 5 displays 6-hourly snapshots of the interaction between MCSs and the mid-latitude jet stream. On 06/13 00 UTC (Fig. 5a), a low pressure system has traversed over the Rockies (not shown) and leads to the development of MCSs. An active MCS is located at 90°W, with a coherent 0 PVU contour located on the northern edge of the MCS, indicating near zero, but negative PV at the tropopause due to diabatic heating associated with MCSs (Hertenstein & Schubert, 1991; Metz & Bosart, 2010). Note the poleward orientation of the irrotational wind field centered on the observed MCS which serves to advect the negtive PV feature radially outwards (Grams et al., 2015). A strong jet streak with wind speeds in excess of 50 m s^{-1} exists directly poleward of the 0 PVU contour. The close proximity of the negative PV to the 2 PVU line facilitates compression of the zonal PV gradient and thus serves to enhance jet stream wind speeds (Stuivenvolt Allen et al., 2021; Grams et al., 2015). During this time, another MCS, termed M1, begins developing east of 110°W and is also co-located with a smaller mesoscale 0 PVU contour.

By 06/13 06 UTC (Fig. 5b), the MCS east of 90°W has propagated eastwards and begun dissipating. The 0 PVU contour persists in spatial extent and advects eastwards along the jet stream. The jet streak propagates downstream following the region where negative PV is within close proximity to the 2 PVU line. M1 has propagated towards the north-east and has rapidly grown in size. The irrotational wind field around M1 has increased in magnitude consistent due to intensification of the MCS over the first 6-9 hours following its genesis (Yang et al., 2017). The negative PV arising M1 is also observed to increase following the intensification of the irrotational wind field.

By 06/13 12 UTC (Fig. 5c), M1 predominantly advects northwards alongside the spatially expanding 0 PVU contours which experience poleward advection and approximately follow the vector direction of the irrotational wind field. Even as M1 begins to dissipate by 06/13 18 UTC (Fig. 5d), the 0 PVU contours persist and agglomerate into a coherent band structure as observed in Clarke et al. (2019). It is worth noting that M1 was a temporally persistent cloud feature with a lifetime of 20 hours according to the FLEXTRKR data. Its prolonged lifetime denotes that this particular MCS was nocturnal.

By 06/14 00 UTC (Fig. 5e), note the close proximity between the 0 and 2 PVU contours. The negative PV's anticyclonic circulation serves to enhance anticyclonic shear (not shown) on the equatorward branch of the the ridge and contributes to enhancements in jet stream wind maxima to values in excess of 60 m s^{-1} due to increasing compression of the isobaric PV gradient (B. Harvey et al., 2020). The poleward motion of the negative PV filament coincides with the northward shift of the 2 PVU line along the equatorward branch of the ridge and is similarly observed in previous negative PV - jet interaction research (Clarke et al., 2019; Oertel et al., 2020).

It is worth mentioning that the persistence of the poleward 850 hPa wind vectors discussed in Fig. 2 will also aid in ridge building via low-level warm-air advection (Maddox, 1983). While quantifying the relevance of each process for ridge building is outside of the scope of this study. The localized perturbation of the jet stream along the equatorward branch of the ridge has previously been identified as a signature of negative PV advection (Clarke et al., 2019; B. Harvey et al., 2020).

By 06/14 06 UTC (Fig. 5f), the 0 PVU contour produced by M1 begins to dissipate. Note its downstream advection causes the jet streak to also propagate downstream. M2 has rapidly developed into a large-scale MCS alongside an intensified irrotational wind field. Note that M2 extends past 52°N; however, due to the domain constraints of FLEXTRKR, the MCS object appears to cut off at this latitude. As with the observations of M1, the 0 PVU contours produced by M2 are advected polewards on 06/14 12 UTC (Fig. 5g) by the irrotational wind field and similarly agglomerate into a coherent band of 0 PVU air by 06/14 18 UTC (Fig. 5h). By 06/15 00 UTC (Fig. 5i), the 0 PVU contour advects closer to the jet stream and propagates downstream under the influence of the jet stream's mean flow. The band of negative PV magnifies another jet streak with wind speeds in excess of 60 m s^{-1}. Thus, the evolution of negative PV arising from M2 is rather analogous to the observations made for M1.
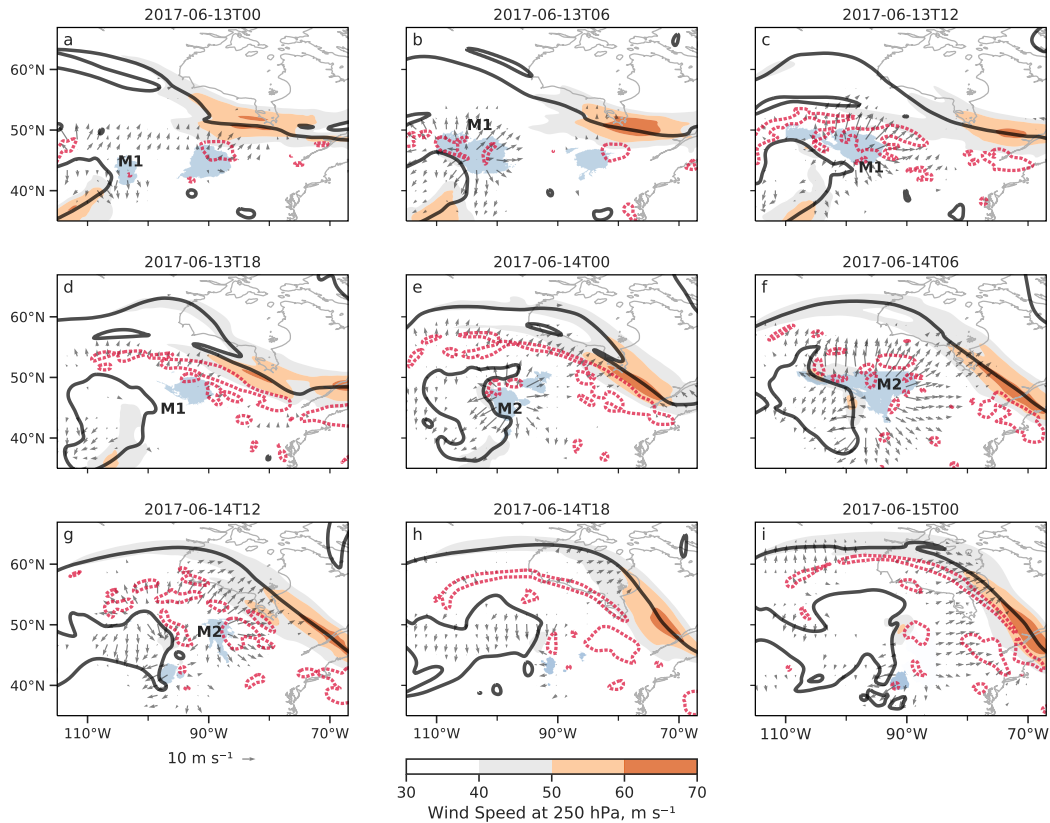
–14–

Figure 5. 6-hourly 250 hPa ERA5 reanalysis examining jet stream modulation by mesoscale convective systems covering the time-period 06/13 00 UTC - 06/15 00 UTC. Blue shading denotes the location of mesoscale convective system objects as identified by the FLEXTRKR algorithm. MCSs of interest are annotated as M1 and M2. The black solid contour denotes the 2 PVU line, it is used as a proxy for the central location of the jet stream. The red dotted contour denotes the 0 PVU line and is used as a proxy for air arising from MCS outflow. The PV contours have been smoothed using a 9-point smoother to filter out noisy 0 PVU contours. The orange shading indicates wind-speeds with units m s^{-1}. Irrotational wind field vectors are plotted where the magnitude is in excess of 5 m s^{-1}

.

4.3 Dynamics over North America: Forecast Model Performance

The poleward advection of negative PV arising from MCSs correspond to jet stream dynamics perturbations. The advection of negative PV towards the jet stream is also co-located with the development of the forecast day-2 WAE discussed in Fig. 4c. To synthesize the relationship between the WAE and the observations of negative PV advection, the model representation of the negative PV filament at 06/14 00 UTC is assessed in relation to the WAE. Using the boxed region outlined in Fig. 4c in the North American domain, the relationship between the 250 hPa day-2, area-averaged PV, relative vorticity, potential temperature and jet wind speed maxima is assessed against the day-2 WAE for each ensemble member. The boxed region during this time is selected as it encapsulates the region of WAE maxima (and ensemble standard deviation maxima) as well as the location of the negative PV feature.

–15–

Fig. 6a denotes the relationship between the WAE metric and PV. At first glance, a linear relationship is observed for each model, although the relationship does show improved linearity when plotting the natural logarithm of WAE, indicating exponential incease in WAE as the area averaged PV increases towards higher values. The interpretation of the results are unchanged depending on the choice of y-axis scale; hence, for simplicity, the WAE is not logged. On average, a reduction of 1 PVU is associated with a 250 m^2 s^{-2} decrease in the WAE when considering all ensemble members. While there is notable ensemble spread in the representation of PV, only 3 ensemble members (from the ECMWF model) produce lower PV in comparison to the ERA5 reanalysis. The ensemble mean of all models is 0.65 PVU larger than in ERA5, indicating that the forecasting models struggle with simulating the low values of the PV field in the boxed region. This result is particularly notable for the KMA in which the mean difference in PV with respect to ERA5 reaches 1 PVU. This result is complimented by the KMA ensemble members having the largest values of WAE.

Given the close relationship between PV and WAE, the relative vorticity field is also examined in Fig. 6b as it is a key variable in the PV equation. The figure similarly illustrates a gentle exponential relationship with a tighter spread pattern compared to Fig. 6a. The WAE is constructed from the relative vorticity and the figure clearly highlights that an increased depature of the relative vorticity from reanalysis serves to enhance the WAE. . The ensemble members with the highest WAE, which tend to be from the KMA model, show minimal anticyclonic flow in the boxed region as the mean relative vorticity approaches positive values. As with Fig. 6a, the ensemble spread is biased towards higher values of relative vorticity compared to the reanalysis.

The isobaric PV equation is also constructed from gradients of the potential temperature field. For simplicity, Fig. 6c shows the relationship of the in−situ potential temperature field at 250 hPa against WAE. Reducing PV at upper−levels is accompanied by increases in the the potential temperature (Haynes & McIntyre, 1987; Teubler & Riemer, 2016). The figure illustrates that potential temperature continues to show a highly linear relationship against WAE for the ECMWF and NCEP models with higher potential temperature being is associated with a reduction in the WAE. In contrast, the JMA and KMA models show no relationship between potential temperature and WAE. A Pearson's test of significance was performed on all four models. The ECMWF and NCEP models both produced p values below 0.05 and a line of best fit was plotted for these two models for clarity. While the ECMWF and NCEP produce a statistically significant linear relationship, most ensemble members continue to fail to produce ERA5's comparatively higher potential temperature.

Fig. 6d illustrates the relationship between the maxima wind speed forecasted within the boxed region and the mean WAE. As with potential temperature, the ECMWF and NCEP models reveal a statistically significant linear relationship between WAE and wind maxima. In particular, the NCEP model demonstrates an extremely linear relationship with a correlation coefficient of -0.88 (and -0.56 for the ECMWF). The results obtained from this relationship are consistent with the results from Fig. 4 in which jet stream wind extrema are co-located with WAE maxima. The results are also in agreement with previous literature observing increases in jet stream wind maxima during instances of negative PV advection using cloud-resolving simulations (Oertel et al., 2020; B. Harvey et al., 2020). As with potential temperature (Fig. 6c), the JMA and KMA do not display a linear relationship to the WAE. An examination of the mean wind speed against mean WAE showed no relationship for any of the models.

An additional investigation (not shown) in which the response of the PV was compared against the relative vorticity, potential temperature and maximum wind speeds indicated a linear relationship for the ECMWF and NCEP models. It was noted that ensemble members which produced the lowest values of PV, also produced the lowest values of relative vorticity, the highest values of potential temperature and the highest jet stream wind maxima values. The JMA and KMA models only show a strong relationship between PV and relative vorticity. While developing further understanding as to why these particular relationships differ between models is outside the scope of the study, it remains clear that the rotational component of PV is closely linked to jet stream wind error in all 4 of the models.

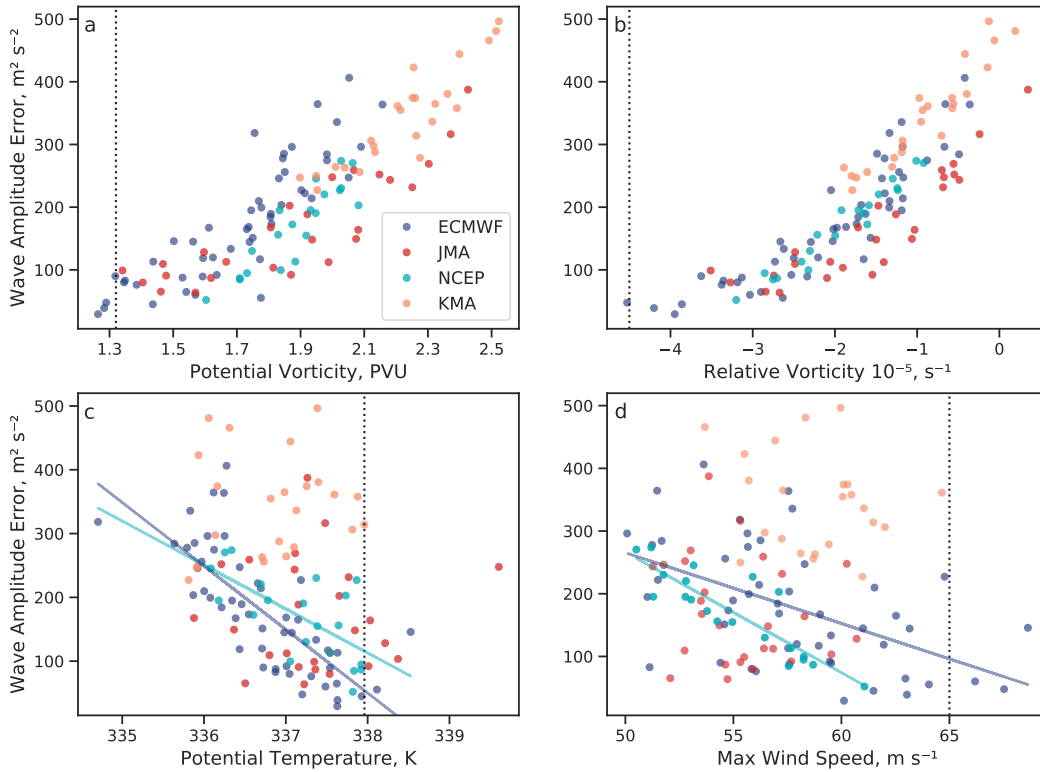**Figure 6.** Relationship between the weighted area-averaged $(54°N, 89°W) – (44°N, 73°W)$ 250 hPa wave amplitude error metric at forecast day-2 and select 250 hPa meteorological fields forecasted at day-2 that are hypothesized to impact rotational wind error within the jet stream. The variables selected include the area-averaged PV (a), relative vorticity (b), potential temperature (c) and the max wind speed (d) within the averaging domain. The relationship is displayed for each ensemble member from each model. The black dotted line denotes the value obtained from ERA5 reanalysis. The solid colored lines denote the line of best-fit for model's that produced a statistically significant ($p<0.05$) relationship against wave amplitude error for the potential temperature and max wind speed. Significance is determined via the computation of a Pearson's Correlation Coefficient.

Given the close relationship between WAE and PV, as well as, between WAE and relative vorticity for all models, it is of interest to visualize what feature within the boxed region serves to introduce WAE into the jet stream. The scatter plot alone does not show whether error in the negative PV features progresses into WAE

within the jet stream or whether some other dynamic feature is influencing WAE within the box region. Figure 7 serves to illustrate the advection of relative vorticity error associated with negative PV. The relative vorticity error is selected to be plotted over PV error as vertical interpolation errors when computing isobaric PV saturate the error signal at higher latitudes (several degrees above the 2 PVU line). The relative vorticity only needs to be computed at a single level, which negates any vertical interpolation errors.

Beginning from 06/13 06 UTC (Fig. 7a), which represents 30 hours into the forecast, negative PV arising from MCSs (Fig. 5b) at 100°W undergoes spatial expansion onto scales resolvable by the datasets used in this study. Anti-cyclonic errors in the relative vorticity field are predominantly located within the contours of negative PV. At 06/13 12 UTC (Fig. 7b), the negative PV experiences poleward expansion as shown in Fig. 5c. Large anticyclonic errors in the relative vorticity field on the order of $\times 10^{-4} s^{-1}$ reside within the negative PV features. Strong cyclonic errors of equal magnitude lie adjacent to the negative PV contours. Much of the error lies across the 50°N latitude band, where the majority of the negative PV resides.

On 06/13 18 UTC (Fig. 7c), the negative PV agglomerates into the banded structure and is advected polewards. Note that the regions of relative vorticity error also propagate within the contours of negative PV and thus also experience poleward advection. The result indicates that the anticyclonic vorticity error (and thus PV error) are closely linked to the negative PV feature. Differences in relative vorticity in excess of $5 \times 10^{-5} s^{-1}$ between ensemble members with the largest and smallest WAE also emerge. The maxima in the ensemble differences predominantly arises in the regions where the negative PV interacts with the jet stream and thus where the PV gradient (as well as relative vorticity gradient) is large.

On 06/14 00 UTC (Fig. 7d), the anticyclonic error within the 0 PVU contour continues to experience advection. The error enhances in magnitude as it reaches the point of closest proximity to the jet stream. Relative vorticity error values in excess of $1.5 \times 10^{-4} s^{-1}$ are observed between the analysis and the ensemble mean. Ensemble spread between the largest and smallest WAE also increases spatially to cover the majority of the negative PV contour. The largest ensemble differences are predominantly located along the poleward facing side of the negative PV feature. Maxima in the anticyclonic error in excess of $1 \times 10^{-4} s^{-1}$ are observed that coincide with the location of WAE maxima (Fig. 4c). The results thus provide confidence that the PV and relative vorticity relationships discussed in Fig. 6 predominantly arise from the representation of the advected negative PV feature and its associated circulation pattern.

The spatial locations of the relative vorticity errors were consistent in all four models. Since the maxima of the anticyclonic relative vorticity error clearly reside within regions of negative PV, this indicates that the representation of the negative PV feature is consistently misrepresented in all four forecasting models. Upon individual examination, the KMA model produces the largest magnitude relative vorticity errors while the JMA produces the lowest. This is consistent with the observed relationship in Fig. 6b. However, these magnitude differences only manifest at later forecast lead-times when the negative PV is in close proximity to the jet stream. This result implies that aside from the origin of negative PV being poorly simulated, its interaction with the jet stream may also be erroneous. For the interest of the reader, Fig. 7 is also replotted for each individual model and provided in the supplementary material (Fig. S1).
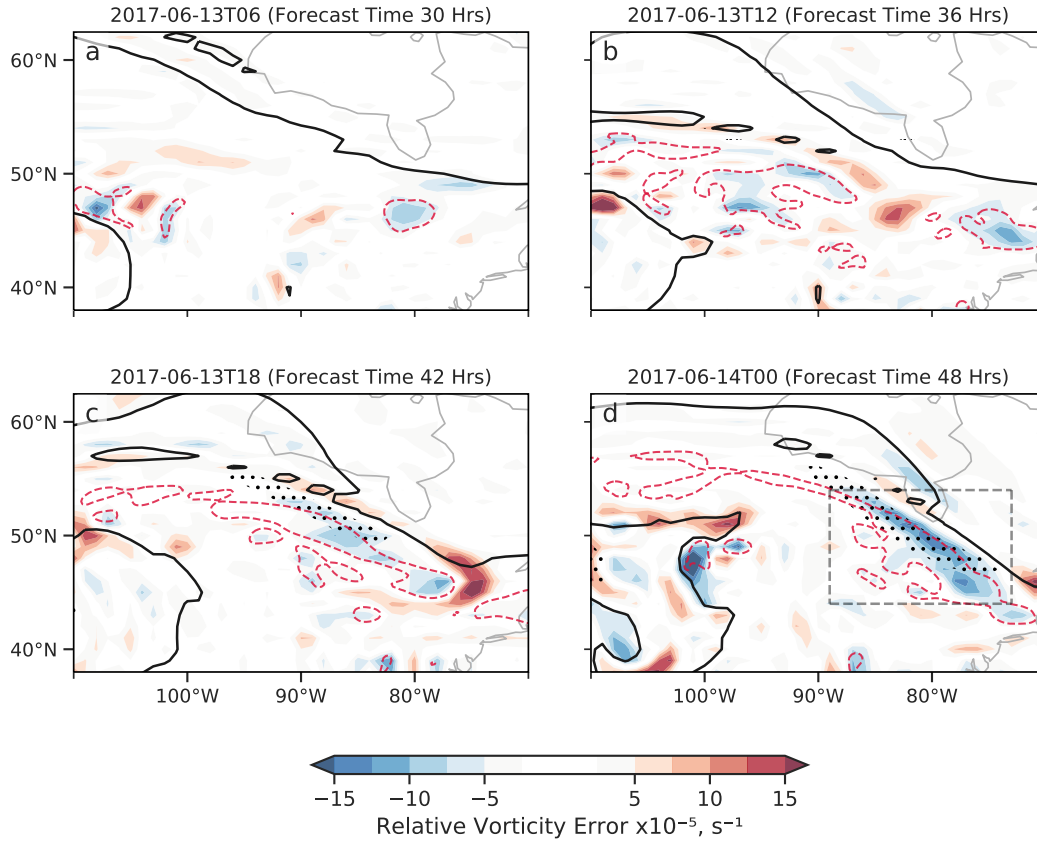
–18–

Figure 7. 6-hourly 250 hPa analysis of relative vorticity error advection. Relative vorticity error is defined as the difference between ERA5 reanalysis and the ensemble mean of all 4 models. Blue shading illustrates negative relative vorticity errors (ERA5 produces a stronger anticyclonic circulation with respect to the forecasting models). Red shading illustrates positive relative vorticity errors (ERA5 produces a stronger cyclonic circulation). The black stippling shows the largest relative vorticity difference between ensemble members with the least WAE (lowest 20th percentile) and most WAE (highest 20th percentile). The stippling denotes where differences are in excess of 5×10^{-5} s. The red-dashed lines denote contours of 0 PVU. The solid black line denotes 2 PVU. The PV data is obtained from ERA5 reanalysis. The gray dashed lines show the North American domain where maxima in the day-2 WAE manifest and the region where the scatter-plot relationship is obtained from Figure 6.

4.4 Ensemble Sensitivity Analysis

To determine the downstream impact that different realizations of the wave amplitude error (and thus negative PV advection) over North America have on the evolution of a RWP, the ESA is computed such that the area-weighted, spatially averaged WAE, in the North American domain (54°N, 89°W) – (44°N, 73°W) at day 2 is correlated to the global Z250 field at later forecast lead-times. The large averaging domain for V250 is selected to capture the entire area over which the low PV air interacts with the jet stream (as discussed in Fig. 5). In Figure 8, the results for the day 2, 4 and 6 ESA are displayed for each model alongside the WAF difference. In contrast to the WAF error plotted in Fig. 4, which consists of the difference between the analysis and ensemble mean, the WAF difference in Fig. 8

₅₂₉ involves separating the ensemble members into two groups: those that produced the
₅₃₀ lowest (20th percentile) day 2 WAE and highest (20th percentile) day 2 WAE over
₅₃₁ the North American domain. The mean of these two groups is computed and their
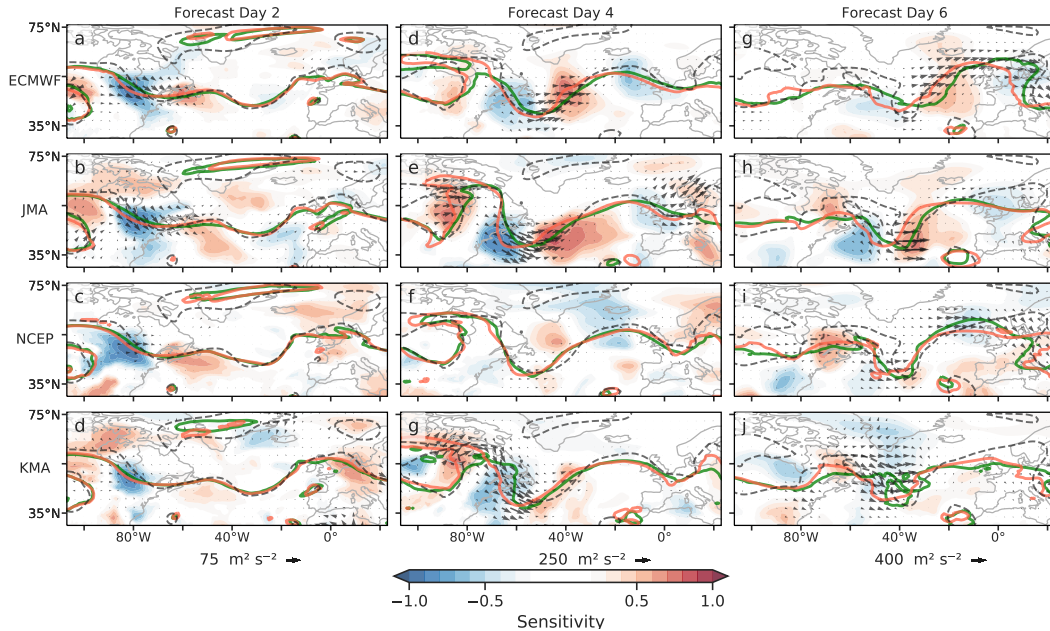₅₃₂ difference is calculated.

Figure 8. Ensemble sensitivity analysis of the day 2 wave amplitude error region (North American domain) at 250 hPa (V250) against global day 2, 4 and 6 Z250. Red (blue) shading indicate positive (negative) correlations between day 2 WAE and day 6 Z250. Each row represents one of the four forecasting models used. The contours show the 2 PVU line. The green (red) line represents the mean of the ensemble members that produced the least (most) amount of day-2 WAE (20th percentile) over the North American domain. The dashed grey line shows the 2 PVU line obtained from the ERA5 reanalysis. Vectors depict the WAF difference between ensemble members with the most and least day-2 WAE
.

₅₃₃ In Figure 8a-d, ensemble members with weaker day-2 WAE over the North
₅₃₄ American domain correlate to higher day-2 Z250 at 80°W, thus indicating that
₅₃₅ models with lower WAE (and thus lower PV values) are associated with a poleward
₅₃₆ perturbation of the 2 PVU line. This relationship is statistically significant in all
₅₃₇ models as Z250 sensitivities in this region reach values in excess of -0.8. All mod-
₅₃₈ els also produce higher Z250 downstream of the North American ridge at 60°W,
₅₃₉ indicative of a modification to the trough-ridge couplet (Zheng et al., 2013). The
₅₄₀ WAF difference denotes maxima ensemble difference in the equatorward branch
₅₄₁ of the ridge for each model. The ECMWF and JMA produce the most extensive
₅₄₂ WAF differences followed by the NCEP and KMA. The WAF difference is orientated
₅₄₃ downstream indicating the flux of wave activity along the jet stream is stronger in
₅₄₄ the ensemble members with less WAE.

₅₄₅ A notable poleward perturbation in the 2 PVU line is seen in the models with
₅₄₆ the least WAE at 80°W (green line). The largest differences exist for the ECMWF
₅₄₇ and JMA models and is consistent with the higher ensemble spread of these models.

–20–

The 2 PVU line produced in the analysis experiences a greater poleward perturbation with respect to the day-2 forecasts. The result suggests that the mechanism for poleward perturbation in this region is rather poorly represented in all models; albeit, less rotational wind error does serve to improve the forecasted location of the 2 PVU line. Other regions that are associated with ridging also reveal poor model performance such as over Europe at 10°W.

For the forecast day-4 plots (Fig. 8d-g), the sensitivity structure over the Atlantic begins differing for each model. The ECMWF and JMA evolve rather similarly indicating a distinct tri-pole sensitivity structure (negative, positive, negative). Examining the differences in the 2 PVU lines between the best and worst performing models shows that the Z250 sensitivity structures appear associated with large-scale phasing differences in the RWP with the best performing 2 PVU line having progressed further eastwards with respect to the worst performing 2 PVU line. The best performing 2 PVU line for the JMA and ECMWF is also in good agreement with the location of the analysis. The KMA also produces a similar sensitivity structure to the ECMWF and JMA over the Western part of the Atlantic but the sensitivity structure is less distinct further east at 40°W. While slight phasing differences are observed in the 2 PVU lines in the KMA at 40°W, a clear phasing difference with respect to analysis begins developing such that the analysis is perturbed further eastwards. A similar relationship to the KMA is observed in the NCEP with clear phasing differences between the forecast and the analysis at 40°W. The longitude locations of sensitivity in the NCEP resemble the ECMWF and JMA model rather closely; albeit, the magnitude of the sensitivity is comparatively weaker.

An examination of the WAF difference shows that the ECMWF performs rather similarly to the WAF maxima location discussed in Fig. 4b. The NCEP also produces WAF difference maxima in the same location as the ECMWF but the lack of ensemble spread means that the WAF difference values are comparatively lower than in the ECMWF. The JMA and KMA also indicate WAF differences in the same location as the ECMWF maxima; however, the JMA and KMA maxima are predominantly located west of the ECMWF and NCEP maxima at 60°W. The location is co-located with large phasing differences in the representation of a trough. These phasing differences are also present in the ECMWF and NCEP but comparatively smaller.

For the day-6 plots (Fig. 8i-l), the ECMWF and JMA indicates an alternating pattern of positive and negative sensitivities that track back from Europe to the Western Atlantic. The alternating sign of these sensitivities illustrates that ensemble members with lower WAE are statistically linked to an eastward progression in the RWP. This result can also be interpreted as ensemble members with a lower value of day-2 PV in the North American domain favoring eastward RWP progression at later forecast times. This result is particularly noticeable at 40°W where differences of 10∘ longitude in the 2 PVU lines are observed between the best and worst performing models. The ECMWF (and to a much weaker extent in the JMA model) also indicate that lower WAE is associated with higher day-6 Z250 over the eastern side of the ridge that has developed over Europe at 10°E. This difference is particularly noticeable in the 2 PVU lines of the ECMWF where the best performing members appear to capture the anticyclonic breaking of the ridge that is also illustrated in the 2 PVU line of ERA5. This particular region was also associated with maxima in the WAE as discussed in Fig. 4c.

The JMA model also indicates that the day-2 WAE modulates phasing differences in the day-6 RWP. The ridge amplification over Europe that is observed in the ECMWF is not visually present in the JMA model as the forecasts of the 2 PVU lines favor a more zonal flow pattern over Europe. The KMA model similarly struggles with representing ridging and indicates a transition towards zonal flow.

–21–

In contrast, the ensemble members which produced the least day-2 WAE in the NCEP model indicate a more amplified day-6 ridge and is associated with a region of statistically significant Z250 sensitivity. The best performing ECMWF and NCEP ensemble members also produce a much stronger WAF over the ridging region, unlike the JMA and KMA, which denote maxima WAF differences arising from the Atlantic trough.

While the day-6 forecasts of each model diverge fairly notably , it is worth pointing out that the location of the sensitivity structures all occur across the same longitude bands stretching from the Western Atlantic to Europe. The ESA thus implies that phasing differences in the day-6 RWP can still be attributed to each model's day-2 WAE (and thus in the representation of the PV field in the North American domain). Furthermore, the ESA was only calculated for an individual MCS despite two other notable MCSs occurring that were associated with negative PV advection towards the jet stream (Fig. 5). Since each model produces a statistically significant sensitivity pattern in the troughs and ridges of Z250, this indicates that the misrepresentation of MCS interactions with the jet stream can have far-reaching effects on the downstream propagation of a RWP. In this case, the full impact of all MCSs on downstream development is not captured through the paradigm of ESA as only one of the MCSs is assessed. Additionally, the ESA in this study only examines the impact of negative PV arising from MCSs, which is noted to be underrepresented in magnitude with respect to reanalysis (Fig. 7).

5 Discussion and Conclusions

The case-study investigates the impact that MCSs have on downstream development via exploiting global ensemble forecast data from various state-of-the-art forecasting centers. In this particular case, the advection of erroneously forecasted negative PV arising from North American MCSs towards the jet stream is shown to influence the forecast of downstream development. Specifically, ensemble members that advected lower values of PV along the equatorward branch of a North American ridge served to exacerbate the eastward progression of a RWP and consequently impinged on forecasted ridge development over Europe. Our results support recent work identifying that the interaction of negative PV arising from MCSs with the jet stream can modulate downstream large-scale atmospheric dynamics (Clarke et al., 2019).

The strength of the anticyclonic circulation associated with negative PV is underrepresented in forecasting models. Relative vorticity errors on the order of $x10^{-4}$ s^{-1} are observed within synoptic-scale regions of negative PV. The study showed that virtually all ensemble members from the four analyzed forecasting models failed to accurately represent the PV field during negative PV interaction with the jet stream. In the case-study by Clarke et al. (2019), the lack of negative PV production associated with an MCS in a global model was attributed to a failure of the model to forecast the MCS. Here, the synoptic set-up and subsequent mesoscale convection (divergence field) was noted to be well forecasted. However, the production of negative PV and its subsequent interaction with the jet stream was poorly simulated. This result suggests that even accurate forecasts of the location of mid-latitude convection in global forecasting models could fail to realistically represent the upscale evolution of negative PV.

A reason for the failure to represent the advection of negative PV towards the jet stream could simply be attributed to the origin of negative PV arising from convective scale heating (Chagnon & Gray, 2009). The upscale evolution of diabatically modified PV is determined by parameterized processes known to be erroneous (Baumgart et al., 2018). Additionally, the large-grid spacings of global forecasting

–22–

models will serve to smooth sharp gradients of PV, such as in mesoscale regions of negative PV (Clarke et al., 2019). This may explain why all of the observed regions of negative PV are associated with large anticyclonic errors. Aggressive damping schemes that target instabilities may also contribute to the observed PV forecast errors. Oertel et al. (2020) and Oertel and Schemm (2021) show that regions of negative PV are analagous to strong inertial instability. Inertial instability is modulated in part by the horizontal vorticity field. The misrepresentation of this instability could also impact the representation and evolution of negative PV in forecasting models.

The assessment of the downstream response to negative PV interaction with the jet stream via ensemble sensitivity analysis indicated a statistically significant modification to the evolution of a RWP. Models that produced the least amount of rotational wind error (and thus lower PV values) along the jet stream favored a statistically significant eastward progression of the RWP. The ECMWF and JMA model, which had the largest ensemble variation in the rotational wind error, were noted to produce the largest phasing differences in the RWP when comparing the best versus worst performing ensemble members. While notable differences existed in the evolution of the RWP and ridge onset over Europe at later forecast lead times, the ECMWF and NCEP models illustrated that the remote impact of MCSs could be attributed to differences in the ridge amplitude over Europe at forecast day-6. Furthermore, the ensemble sensitivity analysis results illustrated that modifications to RWP phasing were consistently produced in all four models in the same locations. Hence, even after several days into the forecast, RWP modifications can be explicitly linked to MCS dynamics even when using different weather prediction models which are characterized by their individual dynamical cores, physics packages and perturbation methods.

The sensitivity results are particularly interesting as they only examined the impact of an individual MCS. The study noted other MCSs that produced negative PV, which subsequently advected towards the jet stream. Thus, it is likely that the accumulated impact of the MCSs on the downstream flow may have further modulated the downstream RWP evolution (Stensrud & Anderson, 2001). Furthermore, since the case-study uses real forecast data (as opposed to studying the upscale impacts of MCSs in isolation), other dynamic features associated with strong ensemble perturbations will have likely impacted the downstream evolution of the RWP and reduce the sensitivity signal that can be attributed to MCSs. One particular dynamic feature of interest was a trough structure that developed at forecast day-4 over the Atlantic. Given that MCSs modified the phasing of the RWP, the forecasted trough development will consequently be impinged upon. Slight perturbations in the location of the trough have been noted to drastically modify adjacent ridge development in previous ensemble sensitivity analysis studies (Berman & Torn, 2019). Hence, it would have been interesting to further examine the impact that MCS perturbations had on trough development over the Atlantic and whether different realizations of the trough (that can be attributed to MCSs) played a role in the observed ridge building over Europe and thus on the heatwave itself.

The more rapid progression of the RWP observed in this study is in contrast to previous literature suggesting that the advection of low values of PV via the irrotational wind field serves to decelerate the propagation of a RWP via low PV air advection towards the poleward branch of a ridge (Rodwell et al., 2013; Steinfeld & Pfahl, 2019). In this study, negative PV experiences North-Eastward advection towards the equatorward branch of the ridge and produces an eastward perturbation. Previous case-studies have also identified that negative PV experiences an anti-cyclonic advection path when in close proximity to

the jet stream (Oertel et al., 2020; Blanchard et al., 2021). Winters (2021) proposed that different components of the wind field, such as the ageostrophic non-divergent component of the wind, can play a more dominant role over the irrotational wind field in determining the advection of low values of PV towards the jet stream. Our case-study illustrates that negative PV arises from regions of strong irrotational wind-fields; however, it would be interesting to expand upon this research further by identifying whether different components of the wind field become more significant as the negative PV is advected further away from the center of the irrotational wind field.

Overall, we show that the remote influence of MCSs can impact the downstream evolution of large-scale circulation patterns. The ease of access to the multi-model TIGGE data and computational inexpensiveness of this study motivates further work on the role of mid-latitude convection on downstream high-impact weather. ESA appears to be a feasible technique to use for further work. However, it should be used with caution when employed on coarse, global forecast data as large-scale negative PV structures appear to be consistently mis-forecasted. The study was not able to diagnose the role of MCSs on the extremity of the heatwave. It is important to reiterate that the results obtained using the methodology in this study only indicate minor changes in the phasing and amplitude of the forecasted RWP as a result of the North American MCS. It is highly unlikely that the single MCS significantly impacted the forecast of ridging over Europe in this case. An examination of a temporally longer set of forecasts as in Stuivenvolt Allen et al. (2021) could be useful in providing a more statistically robust analysis of the impact of persistent mid-latitude convection on recurring RWPs and subsequent temperature extremes. Ongoing work leverages ERA5 data and cloud-resolving simulations to composite the upscale and downstream impacts of negative PV near the the jet stream.

6 Open Research

ERA5 data are available at https://climate.copernicus.eu/ (Hersbach et al., 2020). TIGGE data can be accessed at https://www.ecmwf.int/en/research/projects/tigge (Swinbank et al., 2016). The MCS database (Feng et al., 2019) is stored in the ARM repository https://www.arm.gov/data/data-sources/flextrkr-164.

References

Ali, S. M., Martius, O., & Röthlisberger, M. (2021). Recurrent Rossby wave packets modulate the persistence of dry and wet spells across the globe. *Geophysical Research Letters*, *48*(5), e2020GL091452.

Anderson, C. J., & Arritt, R. W. (1998). Mesoscale convective complexes and persistent elongated convective systems over the United States during 1992 and 1993. *Monthly Weather Review*, *126*(3), 578–599.

Archambault, H. M., Keyser, D., Bosart, L. F., Davis, C. A., & Cordeira, J. M. (2015). A composite perspective of the extratropical flow response to recurring

western North Pacific tropical cyclones. *Monthly Weather Review*, *143*(4), 1122–1141.

Baumgart, M., Riemer, M., Wirth, V., Teubler, F., & Lang, S. T. (2018). Potential vorticity dynamics of forecast errors: A quantitative case study. *Monthly Weather Review*, *146*(5), 1405–1425.

Berman, J. D., & Torn, R. D. (2019). The impact of initial condition and warm conveyor belt forecast uncertainty on variability in the downstream waveguide in an ECMWF case study. *Monthly Weather Review*, *147*(11), 4071–4089.

Binder, H., Boettcher, M., Joos, H., Sprenger, M., & Wernli, H. (2020). Vertical cloud structure of warm conveyor belts–a comparison and evaluation of ERA5 reanalysis, CloudSat and CALIPSO data. *Weather and Climate Dynamics*, *1*(2), 577–595.

Blanchard, N., Pantillon, F., Chaboureau, J.-P., & Delanoë, J. (2021). Mid-level convection in a warm conveyor belt accelerates the jet stream. *Weather and Climate Dynamics*, *2*(1), 37–53.

Chagnon, J. M., & Gray, S. L. (2009). Horizontal potential vorticity dipoles on the convective storm scale. *Quarterly Journal of the Royal Meteorological Society*, *135*(643), 1392–1408.

Chagnon, J. M., Gray, S. L., & Methven, J. (2013). Diabatic processes modifying potential vorticity in a North Atlantic cyclone. *Quarterly Journal of the Royal Meteorological Society*, *139*(674), 1270–1282.

Chang, E. K. M., Zheng, M., & Raeder, K. (2013). Medium-range ensemble sensitivity analysis of two extreme Pacific extratropical cyclones. *Monthly weather review*, *141*(1), 211–231.

Clarke, S. J., Gray, S. L., & Roberts, N. M. (2019). Downstream influence of mesoscale convective systems. Part 1: influence on forecast evolution. *Quarterly Journal of the Royal Meteorological Society*, *145*(724), 2933–2952.

Cooney, J. W., Bowman, K. P., Homeyer, C. R., & Fenske, T. M. (2018). Ten year analysis of tropopause-overshooting convection using GridRad data. *Journal of Geophysical Research: Atmospheres*, *123*(1), 329–343.

Cotton, W. R., Lin, M.-S., McAnelly, R. L., & Tremback, C. J. (1989). A composite model of mesoscale convective complexes. *Monthly Weather Review*, *117*(4), 765–783.

Dawson, A. (2016). Windspharm: A high-level library for global wind field computations using spherical harmonics. *Journal of Open Research Software*, *4*(1).

Feng, Z., Houze Jr, R. A., Leung, L. R., Song, F., Hardin, J. C., Wang, J., . . . Homeyer, C. R. (2019). Spatiotemporal characteristics and large-scale environments of mesoscale convective systems east of the Rocky Mountains. *Journal of Climate*, *32*(21), 7303–7328.

Feng, Z., Leung, L. R., Houze Jr, R. A., Hagos, S., Hardin, J., Yang, Q., . . . Fan, J. (2018). Structure and evolution of mesoscale convective systems: Sensitivity to cloud microphysics in convection-permitting simulations over the United States. *Journal of Advances in Modeling Earth Systems*, *10*(7), 1470–1494.

Fragkoulidis, G., Wirth, V., Bossmann, P., & Fink, A. (2018). Linking Northern Hemisphere temperature extremes to Rossby wave packets. *Quarterly Journal of the Royal Meteorological Society*, *144*(711), 553–566.

Grams, C. M., Lang, S. T., & Keller, J. H. (2015). A quantitative assessment of the sensitivity of the downstream midlatitude flow response to extratropical transition of tropical cyclones. *Geophysical Research Letters*, *42*(21), 9521–9529.

Gray, S. L., Dunning, C., Methven, J., Masato, G., & Chagnon, J. M. (2014). Systematic model forecast error in Rossby wave structure. *Geophysical Research Letters*, *41*(8), 2979–2987.

Grazzini, F., & Vitart, F. (2015). Atmospheric predictability and Rossby wave packets. *Quarterly Journal of the Royal Meteorological Society*, *141*(692), 2793–2802.

Harvey, B., Methven, J., Sanchez, C., & Schäfler, A. (2020). Diabatic generation of negative potential vorticity and its impact on the North Atlantic jet stream. *Quarterly Journal of the Royal Meteorological Society*, *146*(728), 1477–1497.

Harvey, B. J., Methven, J., & Ambaum, M. H. P. (2016). Rossby wave propagation on potential vorticity fronts with finite width. *Journal of Fluid Mechanics*, *794*, 775–797.

Haynes, P. H., & McIntyre, M. E. (1987). On the evolution of vorticity and potential vorticity in the presence of diabatic heating and frictional or other forces. *Journal of the Atmospheric Sciences*, *44*(5), 828–841.

Hersbach, H., Bell, B., Berrisford, P., Hirahara, S., Horányi, A., Muñoz-Sabater, J., ... others (2020). The ERA5 global reanalysis. *Quarterly Journal of the Royal Meteorological Society*, *146*(730), 1999–2049.

Hertenstein, R. F. A., & Schubert, W. H. (1991). Potential vorticity anomalies associated with squall lines. *Monthly weather review*, *119*(7), 1663–1672.

Hoskins, B. J., McIntyre, M. E., & Robertson, A. W. (1985). On the use and significance of isentropic potential vorticity maps. *Quarterly Journal of the Royal Meteorological Society*, *111*(470), 877–946.

Houze, R. A. (2004). Mesoscale convective systems. *Reviews of Geophysics*, *42*(4), RG4003.

Janowiak, J. E., Joyce, R. J., & Yarosh, Y. (2001). A real-time global half-hourly pixel-resolution infrared dataset and its applications. *Bulletin of the American Meteorological Society*, *82*(2), 205–218.

Joos, H., & Forbes, R. M. (2016). Impact of different IFS microphysics on a warm conveyor belt and the downstream flow evolution. *Quarterly Journal of the Royal Meteorological Society*, *142*(700), 2727–2739.

Keller, J. H., Grams, C. M., Riemer, M., Archambault, H. M., Bosart, L., Doyle, J. D., ... others (2019). The extratropical transition of tropical cyclones. Part II: Interaction with the midlatitude flow, downstream impacts, and implications for predictability. *Monthly Weather Review*, *147*(4), 1077–1106.

Keyser, D. A., & Johnson, D. R. (1984). Effects of diabatic heating on the ageostrophic circulation of an upper tropospheric jet streak. *Monthly weather review*, *112*(9), 1709–1724.

Lillo, S. P., & Parsons, D. B. (2017). Investigating the dynamics of error growth in ECMWF medium-range forecast busts. *Quarterly Journal of the Royal Meteorological Society*, *143*(704), 1211–1226.

Lin, Y. (2011). *GCIP/EOP Surface: Precipitation NCEP/EMC 4KM Gridded Data (GRIB) Stage IV Data, version 1.0. UCAR/NCAR Earth Observing Laboratory.* Boulder, Colo.

Maddox, R. A. (1983). Large-scale meteorological conditions associated with midlatitude, mesoscale convective complexes. *Monthly Weather Review*, *111*(7), 1475–1493.

Magnusson, L. (2017). Diagnostic methods for understanding the origin of forecast errors. *Quarterly Journal of the Royal Meteorological Society*, *143*(706), 2129–2142.

Magnusson, L., Chen, J.-H., Lin, S.-J., Zhou, L., & Chen, X. (2019). Dependence on initial conditions versus model formulations for medium-range forecast error variations. *Quarterly Journal of the Royal Meteorological Society*, *145*(722), 2085–2100.

Martínez-Alvarado, O., Madonna, E., Gray, S. L., & Joos, H. (2016). A route to systematic error in forecasts of Rossby waves. *Quarterly Journal of the Royal Meteorological Society*, *142*(694), 196–210.

Metz, N. D., & Bosart, L. F. (2010). Derecho and MCS development, evolution, and multiscale interactions during 3–5 July 2003. *Monthly Weather Review*, *138*(8), 3048–3070.

Oertel, A., Boettcher, M., Joos, H., Sprenger, M., & Wernli, H. (2020). Potential

vorticity structure of embedded convection in a warm conveyor belt and its relevance for large-scale dynamics. *Weather and Climate Dynamics*, *1*(1), 127–153.

Oertel, A., & Schemm, S. (2021). Quantifying the circulation induced by convective clouds in kilometer-scale simulations. *Quarterly Journal of the Royal Meteorological Society*, *147*(736), 1752–1766.

Parsons, D. B., Lillo, S. P., Rattray, C. P., Bechtold, P., Rodwell, M. J., & Bruce, C. M. (2019). The role of continental mesoscale convective systems in forecast busts within global weather prediction systems. *Atmosphere*, *10*(11), 681.

Prince, K. C., & Evans, C. (2022). Convectively-generated negative potential vorticity enhancing the jet stream though an inverse energy cascade during the extratropical transition of hurricane irma. *Journal of the Atmospheric Sciences*.

Quandt, L.-A., Keller, J. H., Martius, O., Pinto, J. G., & Jones, S. C. (2019). Ensemble sensitivity analysis of the blocking system over Russia in summer 2010. *Monthly Weather Review*, *147*(2), 657–675.

Quinting, J. F., & Vitart, F. (2019). Representation of synoptic-scale Rossby wave packets and blocking in the S2S prediction project database. *Geophysical Research Letters*, *46*(2), 1070–1078.

Riboldi, J., Röthlisberger, M., & Grams, C. M. (2018). Rossby wave initiation by recurving tropical cyclones in the western North Pacific. *Monthly Weather Review*, *146*(5), 1283–1301.

Riemer, M., Jones, S. C., & Davis, C. A. (2008). The impact of extratropical transition on the downstream flow: An idealized modelling study with a straight jet. *Quarterly Journal of the Royal Meteorological Society*, *134*(630), 69–91.

Rodwell, M. J., Magnusson, L., Bauer, P., Bechtold, P., Bonavita, M., Cardinali, C., ... others (2013). Characteristics of occasional poor medium-range weather forecasts for Europe. *Bulletin of the American Meteorological Society*, *94*(9), 1393–1405.

Rodwell, M. J., Richardson, D. S., Parsons, D. B., & Wernli, H. (2018). Flow-dependent reliability: A path to more skillful ensemble forecasts. *Bulletin of the American Meteorological Society*, *99*(5), 1015–1026.

Rodwell, M. J., & Wernli, H. (2022). The cyclogenesis butterfly: Uncertainty growth and forecast reliability during extratropical cyclogenesis. *Weather and Climate Dynamics Discussions*, 1–32.

Röthlisberger, M., Frossard, L., Bosart, L. F., Keyser, D., & Martius, O. (2019). Recurrent synoptic-scale Rossby wave patterns and their effect on the persistence of cold and hot spells. *Journal of Climate*, *32*(11), 3207–3226.

Sánchez-Benítez, A., García-Herrera, R., Barriopedro, D., Sousa, P. M., & Trigo, R. M. (2018). June 2017: the earliest European summer mega-heatwave of Reanalysis Period. *Geophysical Research Letters*, *45*(4), 1955–1962.

Steinfeld, D., & Pfahl, S. (2019). The role of latent heating in atmospheric blocking dynamics: a global climatology. *Climate Dynamics*, *53*(9), 6159–6180.

Stensrud, D. J., & Anderson, J. L. (2001). Is midlatitude convection an active or a passive player in producing global circulation patterns? *Journal of Climate*, *14*(10), 2222–2237.

Stuivenvolt Allen, J., Simon Wang, S.-Y., LaPlante, M. D., & Yoon, J.-H. (2021). Three Western Pacific typhoons strengthened fire weather in the recent northwest US conflagration. *Geophysical Research Letters*, *48*(3), e2020GL091430.

Swinbank, R., Kyouda, M., Buchanan, P., Froude, L., Hamill, T. M., Hewson, T. D., ... others (2016). The TIGGE project and its achievements. *Bulletin of the American Meteorological Society*, *97*(1), 49–67.

Takaya, K., & Nakamura, H. (2001). A formulation of a phase-independent wave-activity flux for stationary and migratory quasigeostrophic eddies on a zonally varying basic flow. *Journal of the Atmospheric Sciences*, *58*(6), 608–627.

Teubler, F., & Riemer, M. (2016). Dynamics of Rossby wave packets in a quantitative potential vorticity–potential temperature framework. *Journal of the Atmospheric Sciences*, *73*(3), 1063–1081.

Torn, R. D., & Hakim, G. J. (2008). Ensemble-based sensitivity analysis. *Monthly Weather Review*, *136*(2), 663–677.

Tung, W.-W., & Yanai, M. (2002). Convective momentum transport observed during the TOGA COARE IOP. Part II: Case studies. *Journal of the atmospheric sciences*, *59*(17), 2535–2549.

Weijenborg, C., Chagnon, J., Friederichs, P., Gray, S., & Hense, A. (2017). Coherent evolution of potential vorticity anomalies associated with deep moist convection. *Quarterly Journal of the Royal Meteorological Society*, *143*(704), 1254–1267.

Weijenborg, C., Friederichs, P., & Hense, A. (2015). Organisation of potential vorticity on the mesoscale during deep moist convection. *Tellus A: Dynamic Meteorology and Oceanography*, *67*(1), 25705.

Wernli, H., & Davies, H. C. (1997). A Lagrangian-based analysis of extratropical cyclones. I: The method and some applications. *Quarterly Journal of the Royal Meteorological Society*, *123*(538), 467–489.

Winters, A. C. (2021). Kinematic processes contributing to the intensification of anomalously strong North Atlantic jets. *Quarterly Journal of the Royal Meteorological Society*, *147*(737), 2506–2532.

Yang, Q., Houze Jr, R. A., Leung, L. R., & Feng, Z. (2017). Environments of long-lived mesoscale convective systems over the central United States in convection permitting climate simulations. *Journal of Geophysical Research: Atmospheres*, *122*(24), 13–288.

Zhang, F., Snyder, C., & Rotunno, R. (2003). Effects of moist convection on mesoscale predictability. *Journal of the Atmospheric Sciences*, *60*(9), 1173–1185.

Zheng, M., Chang, E. K. M., & Colle, B. A. (2013). Ensemble sensitivity tools for assessing extratropical cyclone intensity and track predictability. *Weather and forecasting*, *28*(5), 1133–1156.

Zschenderlein, P., Fragkoulidis, G., Fink, A. H., & Wirth, V. (2018). Large-scale Rossby wave and synoptic-scale dynamic analyses of the unusually late 2016 heatwave over Europe. *Weather*, *73*(9), 275–283.